Mixing and axial dispersion in Taylor–Couette flows: the effect of the flow regime

Marouan Nemri, Sophie Charton, Éric Climent

Mixing and axial dispersion in Taylor–Couette flows: The effect of the flow regime

Marouan Nemri [a], Sophie Charton [a,*], Eric Climent [b]

[a] CEA, DEN, DTEC, SGCS, F-30207 Bagnols-sur-Cèze, France
[b] Institut de Mécanique des Fluides de Toulouse (IMFT) Université de Toulouse, CNRS-INPT-UPS, F-31400 Toulouse, France

HIGHLIGHTS

- Coupled PIV–PLIF measurements in a Taylor Couette Column are performed for different flow regimes.
- Direct Numerical Simulations of the experimental flow regimes are presented.
- The effect of the flow regime on the intra- and inter-vortex mixing efficiency is highlighted.
- The axial dispersion coefficients measured by RTD are analyzed in light of the PLIF and DNS results.

ABSTRACT

The paper focuses on mixing properties of different Taylor–Couette flow regimes and their consequence on axial dispersion of a passive tracer. A joint approach, relying both on targeted experiments and numerical simulations, has been used to investigate the interaction between the flow characteristics and local or global properties of mixing.

Hence, the flow and mixing have been characterized by means of flow visualization and simultaneous PIV (Particle Imaging Velocimetry) and PLIF (Planar Laser Induced Fluorescence) measurements, whereas the axial dispersion coefficient evolving along the successive flow states was investigated thanks to dye Residence Time Distribution measurements (RTD). The experimental results were complemented, for each flow pattern, by Direct Numerical Simulations (DNS), allowing access to 3D information. Both experimental and numerical results have been compared and confirmed the significant effect of the flow structure (axial wavelength of Taylor vortices and azimuthal wavenumber) on axial dispersion.

Keywords:
Taylor–Couette flow
Axial dispersion
Mixing
PIV-PLIF
Numerical simulations

1. Introduction

Taylor–Couette devices are used for many engineering applications, such as low shear mixing, chemical reactors, filtration and bioreactors. Indeed, they allow high values of heat and mass transfer coefficients in a simple and tunable geometry. Emulsion polymerization (Kataoka et al., 1995), heterogeneous catalytic reactions (Legrand and Coeuret, 1986), bioreactor applications (Haut et al., 2003; Hill et al., 2006; Dusting and Balabani, 2009), are examples of industrial applications taking advantages of Taylor–Couette flows. Moreover, they are particularly convenient for small-scale applications, involving either high cost materials or hazardous product handling, e.g. for solvent extraction operations (Davis and Weber, 1960). Taylor–Couette device is composed of an inner rotating cylinder within an outer cylinder, possibly at rest, and the flow dynamics is typically characterized by the Reynolds number (or Taylor number), on which the desired transfer properties depend.

However, it is well-known that Taylor–Couette flows evolve towards turbulence through a sequence of hydrodynamic instabilities as the inner cylinder rotation rate increases while the outer one is fixed. These flow instabilities have been the topic of many theoretical, experimental and numerical studies (Coles, 1965; Fenstermacher et al., 1979). Beyond a critical Reynolds number based on the rotating speed of the cylinder, pure azimuthal Couette flow experiences the formation of steady toroidal vortices, so called Taylor Vortex Flow (TVF). The critical condition is given by the Taylor number or equivalently by the Reynolds number (Re_c) based on the gap width e, the inner cylinder linear velocity ΩR_i (where R_i stands for the cylinder radius) and the kinematic fluid viscosity ν. The Reynolds number is defined as:

$$Re = \frac{\Omega R_i e}{\nu} \tag{1}$$

* Corresponding author.
E-mail address: sophie.charton@cea.fr (S. Charton).

http://dx.doi.org/10.1016/j.ces.2015.09.022

At higher Reynolds numbers a secondary instability causes the flow to become time-dependent due to the appearance of an azimuthal wave (deformation of the vortices). This flow state, known as Wavy Vortex Flow (WVF), is characterized by: an axial wavelength λ_x related to the size of the vortices and an azimuthal wavenumber noted m. As Re further increases, the wavy flow appears modulated by additional frequencies (MWVF) and eventually becomes turbulent (TTVF) (Andereck et al., 1985; Bilson and Bremhorst, 2007).

Depending on the engineering application, this multiplicity of flow-states may induce performance variations. This is mainly the case in two-phase separation chemistry where mixing, if not controlled, can have detrimental effects on the process.

2. Mixing in Taylor–Couette flow: state of the art

Determining and modeling the transport properties of Taylor–Couette flows has been the subject of many experimental and numerical studies (Campero and Vigil, 1997; Desmet et al., 1996a, 1996b; Kataoka et al., 1975; Tam and Swinney, 1987; Rudman, 1998). Most of these studies assume rapid azimuthal and radial mixing and are based on a single parameter model to describe the transport of species along the device, e.g. in the axial direction. Kataoka et al. (1975) were the first ones to propose such a model for the TVF regime. Using residence time distribution (RTD) measurements, they concluded that each vortex behaves as an independent cell, assuming no transfer with adjacent vortices. Therefore the system is modeled as a "pure plug flow". This work has been a key reference for subsequent studies (e.g. Legrand and Coeuret, 1983, 1986; Guihard et al., 1989). The assumption of absence of inter-vortex exchange in TVF regime was later invalidated by the same authors. In fact they observed the existence of a weak inter-cell exchange between adjacent vortices. Kataoka and Takigawa (1981) thus proposed a model with Continuously Stirred Tank Reactors in series (CSTR) to achieve a better description.

When a weak axial flow is superimposed to the Taylor–Couette flow (e.g. Poiseuille Taylor–Couette flow), Kataoka et al. (1977) showed that axial dispersion becomes independent of the molecular diffusion coefficient and increases with the axial flow-rate. This was then confirmed ten years later by Enkoida et al. (1989). These more recent experimental results have been modeled assuming plug-flow with axial dispersion (PFD). The latter model was used by (i) Moore and Cooney (1995) and Pudijioni et al. (1992) for TVF regime, (ii) Tam and Swinney (1987) and Enkoida et al. (1989) for turbulent regime, and (iii) Ohmura et al. (1997) over all regimes. Similarly to the CSTR model, this is a one-parameter model, that allows a 1D representation of the flow. This model was used as a reference to establish several correlations for the axial dispersion coefficient, D_x, as a function of the axial Reynolds number (Re_{ax}) and the tangential one (Re). However, the latter correlations, that are summarized in Table 1, are specific to each geometric configuration (in terms of radius ratio η and aspect ration e/L) and are valid only over a limited range of operating conditions.

Such a one-parameter model is not able to take into account the characteristics of the wavy regimes (WVF and MWVF) in which the transfer between vortices is not negligible. Indeed, the appearance of waves traveling along the azimuthal direction breaks the separation surfaces between the counter-rotating cells, thus increasing drastically the rate of exchange between the outer layers of neighboring vortices (Nemri et al., 2014). The inter-vortex exchange becomes as important as the intra-vortex mixing and the commonly used CSTR in series assumption is therefore invalid. To address the case of wavy regimes, Desmet et al. (1996a) proposed another approach. Their RTD measurements showed that a vortex can not be modeled by a perfectly stirred reactor. By changing the location of the tracer injection, they were able to show that convection dominates in the vortex shell and at the vortices boundaries while diffusion dominates within the vortex core. Thus, they proposed a two-parameters model based on two mixing zones: a poorly mixed inner zone (the core) and a well-mixed outer one (the shell). Intra-vortex transport is then governed by a local coefficient K_c and the inter-vortex exchange by a transport coefficient K_i. By varying K_c, the model could be extended to turbulent regimes. Campero and Vigil (1997) used the same approach and improved the model to account for non-ideal mixing in the core region. Indeed, based on experiments, the authors observed that intra-vortex mixing was slow in the TVF and WVF regimes. They have then developed a three-parameters model, inspired by the work of Desmet et al. (1996b), in which the vortices are represented by a serial network of "CSTRs with exchange volumes", where the cell unit corresponds to a vortex while the vortex core represents the exchange volume. The parameters of this model are respectively: the effective dispersion coefficient, the residence time in the exchange volume and the fraction of the total vortex volume occupied by the exchange volume. This model

Table 1
Summary of correlations for the axial dispersion coefficient D_x.

Authors	$\eta = \frac{R_i}{R_e}$	e (mm)	Re_{ax}	Correlations	Models
Kataoka et al. (1975)	0.75	10	0–90	–	Plug-flow reactor (TVF regime)
Kataoka et al. (1977)	2	20	0–35	$D \propto Re_{ax}^{1.7}$	CSTR in series
Tam and Swinney (1987)	0.494–0.875	3.2–12.85	0	$D_x \propto Re_\theta^\alpha$	1D PFD model (turbulent regime)
Enkoida et al. (1989)	0.593–0.76	18–30.5	60–250	$D_x \propto c_1 Re_\theta^{0.81} + c_2 Re_\theta Re_{ax}$	1D dispersion-convection
Pudijioni et al. (1992)	0.15	1.5	0.03–5.5	–	1D PFD model
Moore and Cooney (1995)	0.73–0.96	0.4–3.8	0.5–30	$D_x \propto Re_\theta^{1.05} Re_{ax}^{0.17}$	1D PFD model
Desmet et al. (1996a)	2.4	24	0	–	2D model: PFD et CSTR
Ohmura et al. (1997)	1.84	18.4	0	$D_x \propto Re_\theta^{2.8}$ (TVF regime) $D_x \propto Re_\theta^{1.5}$ (WVF regime) $D_x \propto Re_\theta^{0.9}$ (turbulent regime)	1D PFD model
Campero and Vigil (1997)	0.875	1.6	0.5	–	2D CSTR with exchange volume (TVF and WVF regimes)
Zhu et al. (2000)	0.875	1.6	0.5	–	2D CSTR with exchange volume
Racina et al. (2010)	0.68–0.758	18.5–12.1	1	$D_x \propto c_1 \eta^{-1.75} Re_\theta^{1.25}$ (WVF regime) $D_x \propto c_2 \eta^{-1} Re_\theta^{0.57} Re_{ax}^{0.25}$ (turbulent regime)	2D CSTR with exchange volume

was also used by Zhu et al. (2000) to show the shortcomings of the classic CSTR model.

The different models found in the literature, and the results obtained in terms of axial dispersion are summarized in Table 1.

It appears from this literature review that, despite the large number of studies on axial mixing in Taylor–Couette flows, there is no consensus between the different models proposed to predict the axial dispersion evolution. The many available correlations were obtained for different flow regimes and different geometrical configurations, and cannot be used to predict the behavior of other configurations. The study we propose contains new information on the intrinsic relation between local mixing and global axial dispersion.

In the present study, we investigate axial dispersion in Taylor–Couette flow patterns from both local and macroscopic points of view. We focus on the mixing mechanisms controlling the axial dispersion in wavy regimes since either numerical (Rudman, 1998; Nemri et al., 2013) or experimental (Nemri et al., 2013) studies have revealed a significant effect of the wavy flow state on axial dispersion. Our objective is to investigate the relation between the dynamics of the flow (e.g. the fluid mechanics perspective) and axial dispersion (the chemical engineering model). In this aim, complementary experimental and numerical tools have been used in order to get better insights on how the local Taylor–Couette flow properties influence the overall mixing behavior (Section 3):

- Flow visualizations, in order to characterize the flow regimes and to define start-up procedure enabling their reproducibility
- Particle Imaging Velocimetry, in order to define accurately the properties of these flows and validate numerical simulations
- Laser Induced Fluorescence, in order to access directly the transport mechanisms responsible for axial mixing
- Measurement of Residence Time Distribution, to quantify axial mixing as a macroscopic quantity
- Direct Numerical Simulations, to complement the experimental investigation with 3D information, and at the end, to predict axial dispersion for each flow regimes achieved in our experiments.

3. Description of experimental techniques and simulations

3.1. Taylor–Couette apparatus

A Taylor–Couette column consists in two concentric cylinders. We will consider only the case where the inner cylinder is rotating and the outer one is at rest. Two different geometrical configurations were used in this study. Each geometry is characterized by its radius ratio η and its aspect ratio Γ. The main features of the two experimental devices are shown in Fig. 1 and details are given in Table 2. The first device, characterized by a large radius ratio, is typical of the miniaturized columns used in the nuclear industry for R&D studies in solvent extraction (Lanoë, 2002). It was mainly used for axial dispersion measurements. The second one, with a smaller radius ratio, was specifically designed for optical measurements (PIV-PLIF, see Nemri et al., 2014).

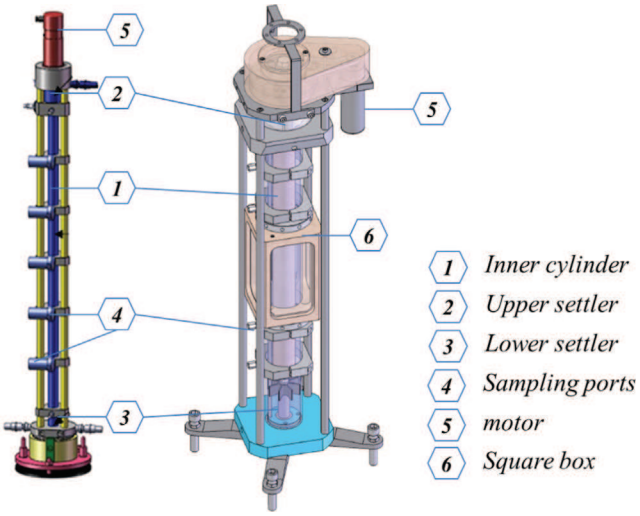

Fig. 1. Schematic presentation of the apparatus: Left: 1st prototype (η=0.85) – Right: 2nd prototype (η=0.687).

The uncertainty on the Reynolds number due to the variation of the inner cylinder speed, fluid viscosity, and other factors was at most 5%. In order to ensure reproducibility of the experimental results, the inner cylinder is driven by a reduction motor guided by a speed regulator system. A ramp generator controls the rotor acceleration during the transient evolution to the desired Reynolds number. Indeed, as highlighted by Coles (1965) and Dutcher and Muller (2009), for a given Reynolds number, the use of different acceleration ramps may lead to various flow states. Therefore, for the two configurations under study, different wave regimes were reproducibly achieved by selecting one of the following start-up protocol:

- An impulsive start from rest to the target rotation rate.
- A gradual acceleration from rest to the desired rotation speed at a constant rate during 300 s.
- A gradual deceleration from a specified rotation speed (Re_0) in turbulent regime to the desired rotation speed at a constant rate during 5 s.

For each of these prescribed procedures, reproducibility was demonstrated and the flow pattern was visualized using an aqueous solution seeded with Kalliroscope AQ-1000 flakes in order to fully characterize the different wavy regimes. Moreover, a spectral analysis of the data was performed to determine the wave state (axial and azimuthal wave numbers) (Nemri et al., 2013).

3.2. Direct Numerical Simulation

Simulations are carried out with a finite volume approach to solve directly the Navier-Stokes equations. Flow regimes under investigation are characterized by low to moderate Reynolds numbers, therefore no turbulence modeling is required. The numerical code JADIM has been developed and validated on many configurations for several years (Calmet and Magnaudet, 1997; Climent and Magnaudet, 1999). The fluid is assumed to be incompressible and Newtonian with constant physical properties. The Navier–Stokes equations then write:

$$\nabla \cdot \mathbf{u} = 0 \tag{2}$$

$$\rho\left(\frac{\partial \mathbf{u}}{\partial t} + \mathbf{u} \cdot \nabla \mathbf{u}\right) = -\nabla P + \mu \nabla^2 \mathbf{u} \tag{3}$$

Table 2
Apparatus geometry and operating conditions.

Parameters	1st prototype	2nd prototype
Inner cylinder radius (R_i)	8.5 mm	24 mm
Outer cylinder radius (R_e)	10 mm	35 mm
Gap width (e)	1.5 mm	11 mm
Radius ratio ($\eta = R_i/R_e$)	0.85	0.687
Length (L)	720 mm	640 mm
Aspect ratio ($\Gamma = L/e$)	480	50
Rotation speed (Ω)	80–1600 rpm	4–1000 rpm
Re range in water	107–2136	111–27,646

where ρ is the fluid density and μ the dynamic viscosity. Gravity effect has been lumped within the pressure contribution (the hydrostatic distribution does not have any effect on the flow dynamics). The code is based on a finite volume method, and the velocity and pressure ($\mathbf{u}$,P) are discretized on a staggered non-uniform cylindrical grid. The numerical code has been already used in laminar and turbulent configurations (see details in Chouippe et al., 2014). The spatial derivatives are computed with second order accuracy, and temporal integration is achieved by a third order Runge–Kutta scheme and a semi-implicit Crank–Nicolson scheme for the viscous terms. Incompressibility is achieved by a projection method associated to a Poisson equation for the pressure correction. Time step is defined in order to have Courant–Friederichs–Lewy number (CFL) lower than 1.

The numerical domain is dimensionless: all flow-related quantities are scaled using the external radius R_e and the reference velocity ΩR_i so that $R_i=\eta$, $R_e=1$ and $\Omega R_i=1$ (see Fig. 2). A uniform mesh is used in both the axial and the azimuthal directions, while the grid is stretched in the radial direction to better resolve stronger velocity gradients near the walls. Periodic boundary conditions are used in the axial direction. An analysis of grid convergence of the simulation results have been carried out to select the appropriate mesh grid ($128\times64\times64$ in the axial, radial and azimuthal directions, respectively).

For the sake of comparison with the experimental results, the following procedure was used to reproduce the exact same flow regimes as those achieved experimentally. Simulating the entire experimental height of the Taylor–Couette device is prohibitive in terms of CPU requirements. Pattern selection is function of geometric properties (aspect ratio of the simulation domain and dimensionless gap width), the Reynolds (or Taylor) number and the flow history. Therefore, to emulate an experimentally observed flow state we impose the observed axial wavelength to the simulation domain and trigger the instability arising in the azimuthal direction. Since the axial wavelength may vary in the range $2\le\lambda_x/e\le3$ depending on the Re value (see Chouippe et al., 2014), the height of the numerical domain was fixed to the desired axial wavelength, *i.e.* $L=\lambda_x$. Note that for Lagrangian simulations (see below) the numerical domain was extended to $L=3\times\lambda_x$ to have a better insight of inter-vortex phenomena. On the other hand, the selection of the azimuthal wave number m was achieved by adding a sinusoidal perturbation to the instantaneous axial velocity component, u_x, in the middle of the gap, during the first few time steps. This perturbation is written in the form:

$$u_x=U_x+A\cdot\cos(m\theta) \tag{4}$$

where the amplitude A correspond to $U_{max}/10$ and m is the desired azimuthal wave number. If the flow regime is wavy, then the perturbation starts to grow and saturates when the flow is established. The two geometries described in Section 3.1 were considered in the numerical study ($\eta=0.85$ and $\eta=0.687$), and for each of them, all the experimentally observed regimes have been reproduced numerically, with their own wave-states.

Besides the determination of the velocity components and flow properties, DNS were coupled to Lagrangian tracking of fluid elements to investigate the mixing mechanisms. In this aim, we considered the trajectories of tracer particles, adequately seeded in the computational domain (either randomly or in well-defined zones).

The method proposed by Rudman (1998) was used to quantify the axial transport. An "effective particle diffusion coefficient", based on the chaotic advection of a large number of fluid particles, is derived from Lagrangian transient simulations. From 1000 to 10,000 markers are randomly seeded throughout the computational domain, which trajectories are tracked over time. Because the motion of fluid elements is mesh free, fluid velocities are interpolated at the positions $x_i(t)$. These particles, advected by the fluid flow, are conveyed gradually from vortex to vortex yielding axial dispersion. The latter is quantified by the following equation:

$$D_x^*=\lim_{t\to\infty}\frac{1}{N}\sum\frac{(x_i(t)-x_i(t_0))^2}{2t} \tag{5}$$

where:

- D_x^* is the effective dispersion coefficient
- N is the total number of fluid elements
- $x_i(t)$ is the axial position of the i^{th} particle at time step t
- $x_i(t_0)$ its initial position

The dimensional dispersion coefficient D_x, in $m^2\,s^{-1}$, is related to the dimensionless coefficient D_x^* by

$$D_x=\frac{Re}{1-\eta}\nu D_x^* \tag{6}$$

3.3. Residence Time Distribution measurements (global mixing)

A spectroscopic method was used to perform RTD measurements of an inert dye. This method has several advantages, as compared to the electro-chemical method used by Raguin et al. (2001), the most important one being that it avoids sensors insertion into the column which may disturb the flow. Indeed, the tracer concentration is monitored by two optical probes placed outside the transparent column. This method also provides the possibility to achieve measurements at different heights along the column. Such a colorimetric method has been used by Desmet et al. (1996a) in their study. However, while the $\eta=0.85$ column has a reflective stainless-steel rotor, the $\eta=0.687$ device, designed for optical measurements, is provided with a non-reflective polycarbonate rotor, thus preventing us from performing spectroscopic measurements in this large-gap configuration. Hence, all the experimental D_x values presented in this paper will be related to the $\eta=0.85$ column.

The principle of RTD experiments is described in Nemri et al., 2013. While the fluid (water or 0.5 M nitric acid solution) is steadily flowing within the annular gap, the tracer (methylene blue) is injected using a syringe through a septum, in a T-valve system located upstream in the fluid circuit. When the injection is located

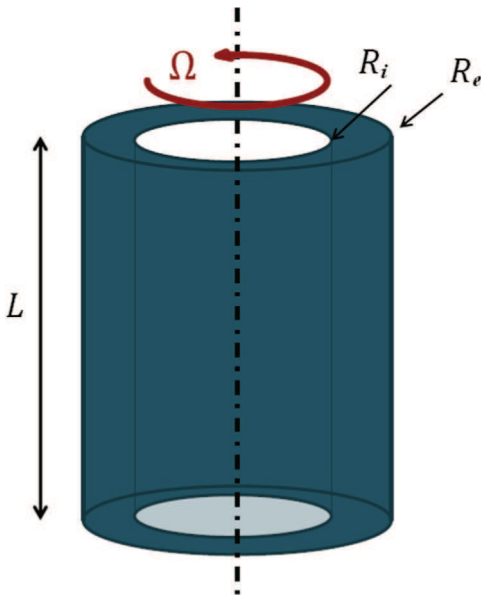

Fig. 2. Geometry of the computational domain and used notations.

at the upper settler, it avoids the risk of diffusion-driven transport of dye in the reverse flow direction, which can be significant when the injection is performed directly within the annular gap (up to a few centimeters). The first sensor is located directly downstream the injection, beneath the settler, while the second one is positioned downstream the first sensor at a given distance between the two probes. The two sensors are identical. The amount of dye injected was chosen in order to ensure a linear dependance of the absorbance with the concentration, in agreement with the linear domain of the Beer–Lambert law. Hence, once normalized, the absorbance evolutions, which are recorded by the sensors during the experiment, give direct access to RTD. The axial flowrate for RTD measurements has been fixed at 100 mL/h. While we tested that up to 300 mL/h no significant effect on flow bifurcations and axial dispersion is observed.

Most studies on axial transport in single-phase Taylor–Couette flow are based on either the PFD or on the CSTR series model to interpret tracer response curves and to determine the effective axial dispersion coefficient by numerical identification of experimental measurements (Tam and Swinney, 1987). However, as already mentioned, even for these single-phase systems, such models are not always suitable, especially at Taylor numbers below the onset of turbulence (Campero and Vigil, 1997; Desmet et al., 1996a).

In this paper, a theoretical model based on the specie's mass balance in a PFD reactor is used. Numerical fitting to experimental RTD and the corresponding theoretical model's prediction leads to the dispersion coefficient (Fig. 3). Since it was not possible to achieve Dirac-type signal at the point where the first probe is located, the theoretical curve we considered for the identification procedure is the one obtained by convolution of the signal recorded on the first probe with the impulsional response characteristic of the plug flow with axial dispersion, thus assimilating the inlet signal to an infinity of Dirac (Villermaux, 1993).

To test the reproducibility of our measurements and estimate the experimental errors, some tests were replicated 15 times. The results have evidenced an excellent reproducibility of the measured D_x value, insofar as a preset startup protocol is used. Thus, for all regimes studied (TVF, WVF, MWVF), the maximum experimental deviation is ranging from 5% to a maximum of 13% .

3.4. Synchronized PIV–PLIF measurements (local mixing)

The local flow properties and mixing mechanisms have been characterized by means of simultaneous PIV and PLIF measurements. A detailed description of the experimental set-up, shown in Fig. 4, is given in Nemri et al. (2014). For the PIV and PLIF measurements, a square chamber was placed outside the glass cylinder and filled with the working fluid to reduce the refraction effects caused by the curved surface of the cylinder. The fluid, an aqueous solution of KSCN (concentration 64% weight, $\rho = 1400\ \mathrm{kg\,m^{-3}}$, $\mu = 2.4 \times 10^{-3}$) which refractive index matches the one of the column wall, was seeded with silver-coated hollow-glass spheres for PIV measurements, whereas a fluorescent tracer consisting of Rhodamine WT was injected for the PLIF experiments.

A PLIF system was used to measure the concentration across the meridional plane ($r-x$) of the gap where x stands for the axial direction and r for the radius one, while the PIV system was used to determine simultaneously the flow regime, measure the velocity field, and track the motion of the vortex boundaries (wavy regimes). We used a dual ND: YAG laser (2×200 mJ, $\lambda = 532$ nm) to illuminate the measurement plane. LIF images were recorded using an sCMOS camera with 2560×2160 pixels and a high-pass optical filter ($\lambda > 540$ nm) suited to the dye emission spectrum. A fluorescent tracer consisting of Rhodamine WT was carefully injected, over approximately 10 s, into the flow through an orifice at the center of the test rig. Rhodamine WT has a maximum absorption wavelength at 565 nm, a maximum emission wavelength at 585 nm and a low temperature and pH sensitivity. So it is particularly suitable for this application. A software and a timing box were used to synchronize the laser with the camera and the PIV system.

For PIV measurements, particle field images were recorded using a PCO.2000 camera with a CCD captor of 2048×2048 pixels and a narrow band-pass optical filter around 532 nm. A telecentric lens was mounted on the camera to avoid parallax distortion along the narrow annulus (this prevents any spurious projection of the azimuthal velocity in the radial plane of measure). The working fluid was seeded with silver-coated hollow glass spheres with density $1.4\ \mathrm{kg\,m^{-3}}$ and an average diameter of 10 µm. Those particles are neutrally buoyant in KSCN at the concentration we used for index matching. Because of the limited front lens diameter of the telecentric lens, the illuminated measurement plane was set to $5.7 \times e$ in the axial direction to make sure that at least two full vortices are captured. Typically, 500–800 image pairs were acquired at 10 Hz, corresponding to the passage of 8–18 azimuthal waves. Velocity vectors were calculated on a square grid (16×16) with sub-pixel inter-correlation.

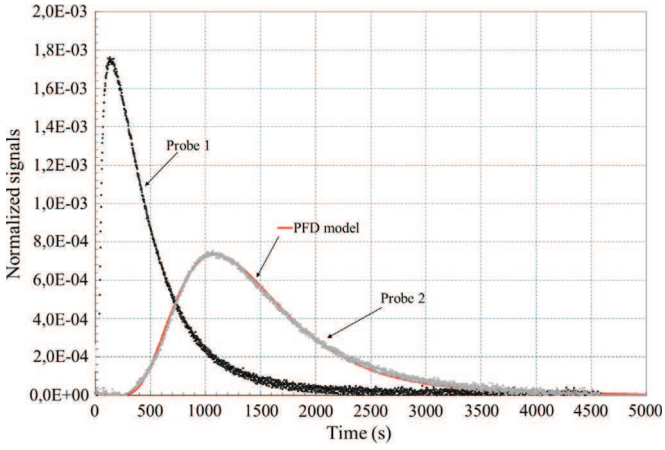

Fig. 3. Example of RTD results and corresponding PFD model's response.

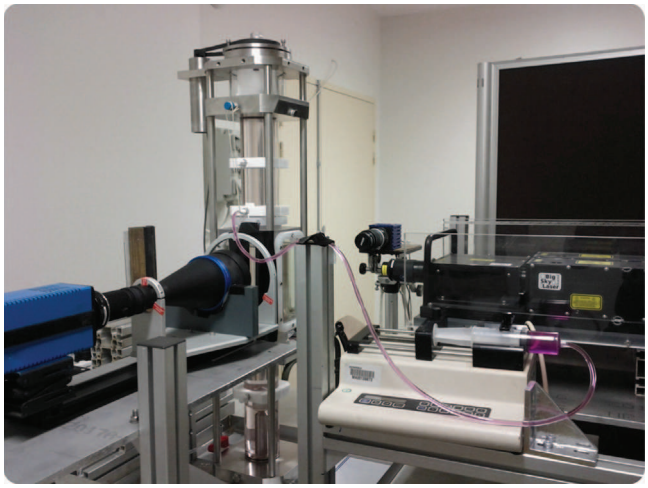

Fig. 4. Experimental set-up for synchronized PIV-PLIF measurements including: a syringe-pump for rhodamine injection and the ND:YAG laser (on the right), a CCD camera with telecentric length for PIV (front), a sCMOS camera for PLIF (rear), and the Taylor–Couette column $\eta = 0.687$ (center).

4. Results and discussion

4.1. Validation of DNS results

First of all, the PIV results were used to validate the DNS simulations (typical velocity fields obtained from PIV measurements are presented in Fig. 5). In this aim, the axial and radial velocity components, U and V, were made dimensionless with the inner cylinder velocity ΩR_i as a reference.

The mean velocity profiles obtained from PIV measurements and DNS simulations are compared in Fig. 6 at three different locations that are relevant for the mixing study: the center of a vortex, and two consecutive vortex boundaries where the fluid is ejected toward either the inner cylinder (inflow zone) or the outer one (outflow zone). An excellent agreement can be observed in every cases representative of the different Taylor–Couette flow regimes we investigated. Moreover, beyond the mean flow values, a good agreement is also achieved regarding velocity fluctuations (Fig. 6, bottom), where deviation is only observed in the near-wall regions presumably due to measurement issues in the curved areas. The maximum of spurious velocities we measured was of the order of 1% of the inner cylinder speed regarding axial component; and 2% for the radial component.

4.2. Taylor–Couette flow properties

In the following, these features of the flow regimes, obtained from DNS simulations, are compared to experimental evidences regarding mixing. The various flow regimes achieved in the two columns, following the start-up procedures given in Section 3.1, have been all reproduced numerically. Examples are shown in Figs. 7 and 8. These figures highlight the succession of instabilities undergone by the flow as the Reynolds number is increased, and give first insights on how the flow may influence mixing. The Reynolds numbers corresponding to the first transitions (Couette $\mapsto$ TVF and TVF $\mapsto$WVF) are given in Table 3 for the two configurations.

In TVF regime (case (a), see also Fig. 5, top), the large scale structures, corresponding to the Taylor vortices, and regularly stacked in the axial direction, can be identified. The instantaneous velocity fields exhibit no significant motion of the vortices boundaries, and no deformation of the shape of each vortex can be observed. The average axial wavelength is approximately $\lambda_x = 2.01$ e which is classic for this flow regime and in agreement with our experiments.

The transition to the wavy regime (WVF, see also Fig. 5, middle) results in the appearance of an azimuthal wave. Lines of cell separation are no longer perpendicular to the axial direction, but exhibit oscillations that affect the entire vortex (case (b)). From there, the flow has a double periodicity identified by an axial wavelength (λ_x) and one or two azimuthal wavenumbers (m), depending on whether the inflow and outflow boundaries have the same period (Fig. 7) or not (Fig. 8). The instantaneous velocity fields hence oscillate both axially and radially. Consequently, over one period of the oscillation, the volume of each vortex is alternately increasing and decreasing, as it periodically fills up with fluid from the adjacent cells, and then shrinks while transferring fluid to its neighbors. Wereley and Lueptow (1999) have described in details the characteristics of this three-dimensional flow, focusing on axial transport.

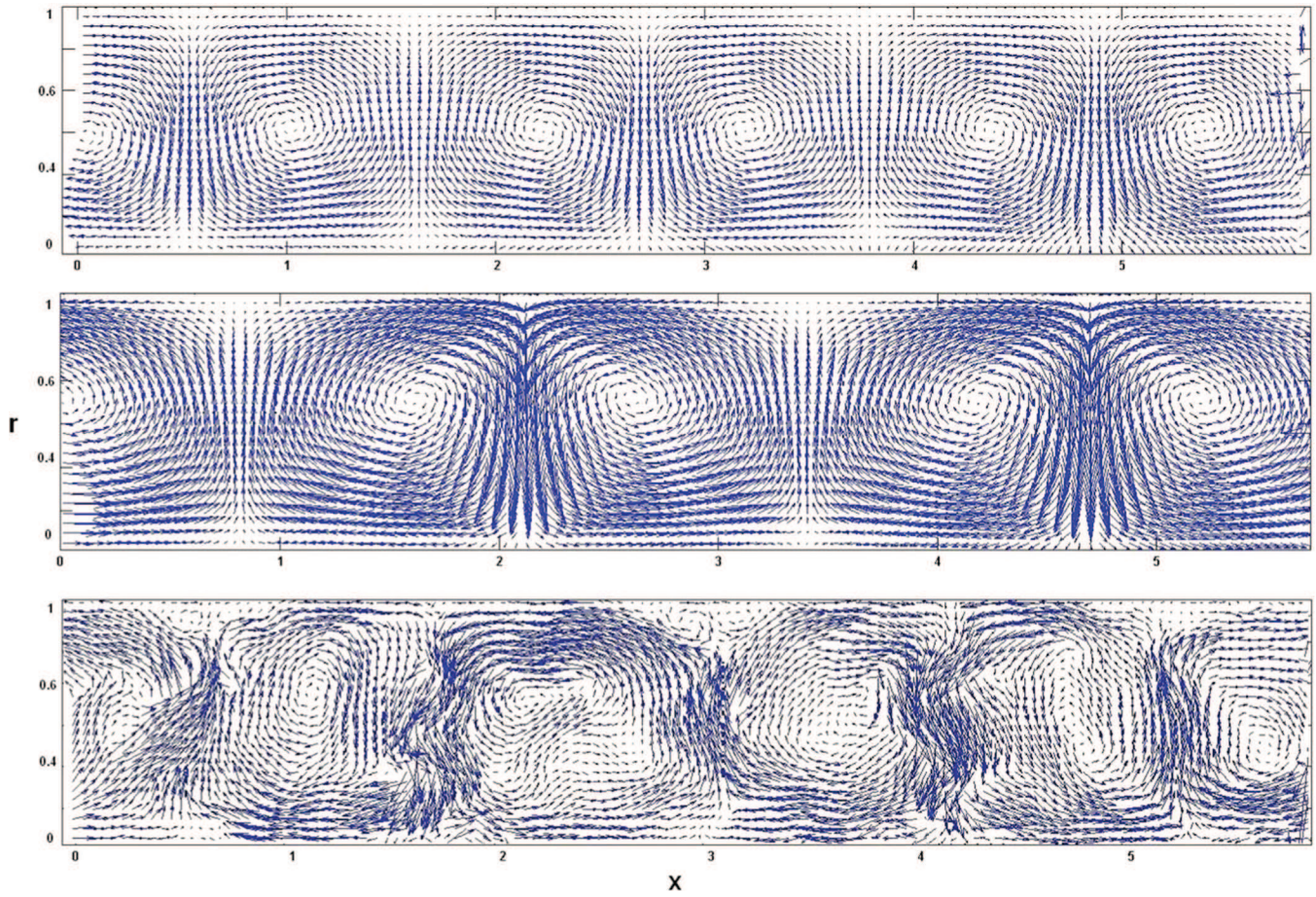

Fig. 5. Instantaneous velocity fields in the $(r-x)$-plane measured by PIV ($\eta = 0.687$). From top to bottom: $Re = 80$ (TVF), $Re = 636$ (WVF), and $Re = 6000$ (TTVF).

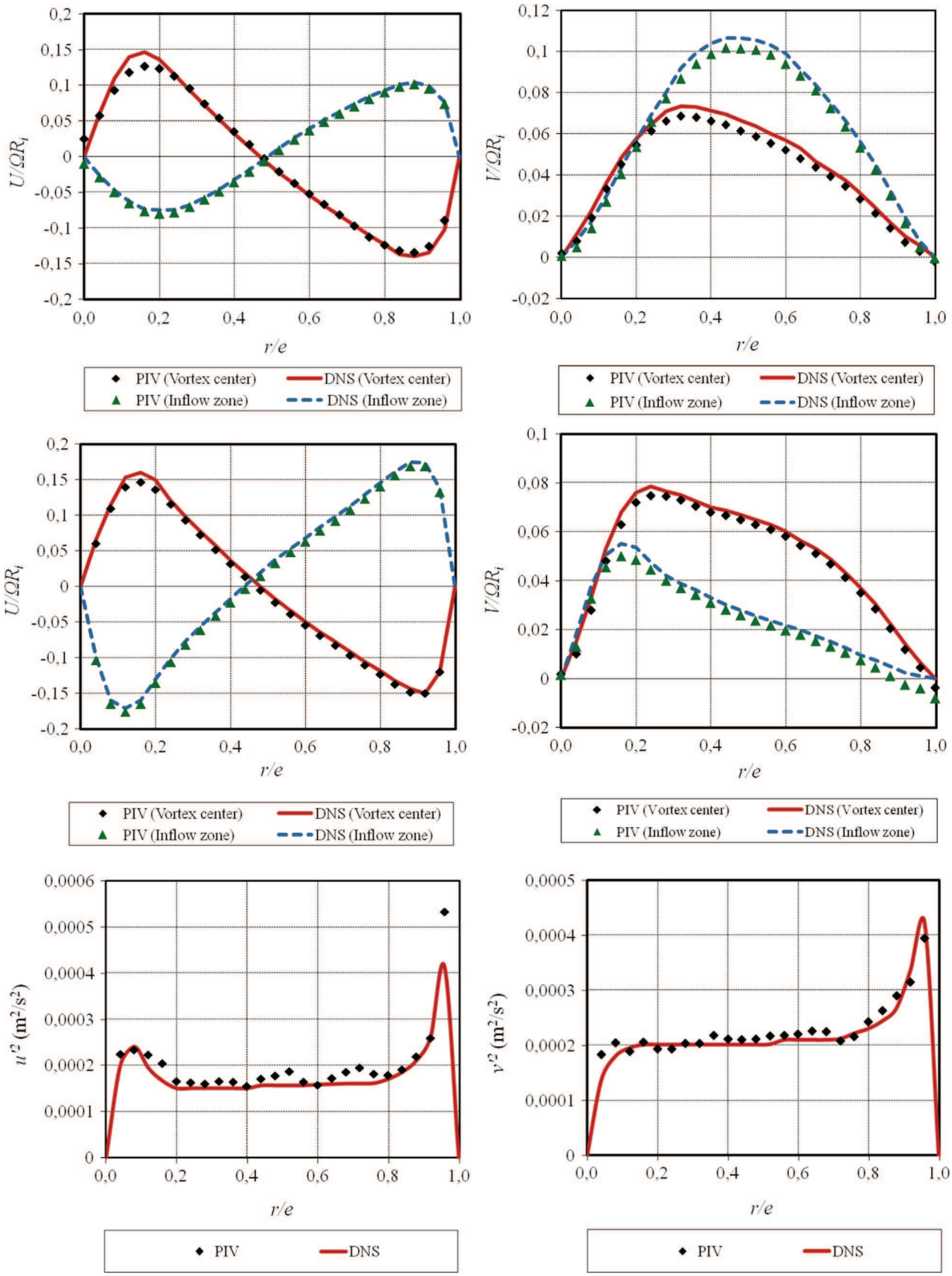

Fig. 6. Comparison between experimental (PIV) and simulated (DNS) results. From top to bottom: Velocity profiles in TVF (Re=318) and WVF (Re=953) regimes, and RMS profiles in TVF regime.

Both DNS and PIV results exhibit this deformation of the vortex induced by the appearance of the azimuthal wave. The wavy perturbation has two main effects on the flow properties. First, the loss of the rotational symmetry causes the velocity field to be dependent on the three spatial coordinates. Second, it breaks the stream surface between neighboring vortices, thus enabling fluid bundles to cross the boundary between vortices, as evidenced by Akonur and Lueptow (2002). Unlike TVF regime, regions of chaotic advection and mixing appear.

When the third instability is reached (MWVF), a modulation of the wave amplitude is developing. An asymmetry in the initially perfectly regular wave train appears and the flow becomes more complex (Figs. 7(c) and 8(c)). The transition to turbulent regime is accompanied by the appearance of turbulent spots that fully seed the Taylor vortices (case (d), see also Fig. 5, bottom).

The flow sequences observed for the two geometries are illustrated in Fig. 9. In agreement with DiPrima et al. (1984) findings, we observed that the lower the aspect ratio, the larger the range of stability of the axi-symmetric TVF regime, and the lower the extent of the MWVF regime.

4.3. Axial dispersion as an indicator of global mixing

The axial dispersion coefficients have been derived from RTD measurements performed on the small-gap column ($\eta = 0.85$). They are plot against *Re* in Fig. 10, where a large scattering of the values can be observed. Moreover, as already highlighted by many authors in the literature (Tam and Swinney, 1987; Kataoka et al., 1977; Enkoida et al., 1989; Moore and Cooney, 1995; Pudijioni et al., 1992), D_x does not appear to vary monotonically with *Re*. The measured values of D_x are particularly scattered in the range where wavy regimes occur and multiplicity of wave states is likely to occur for the same *Re* ($160 < Re < 1600$).

Local mixing mechanisms have been further investigated in order to explain the large scattering observed within the measured D_x values although our experimental data have only a few percents variation related to reproducibility.

4.4. Experimental investigation of mixing mechanisms

Experimental results in Fig. 10 may vary by a factor 2 for the same Reynolds number and various wave states. Rudman (1998) had also reported similar trend with a factor 1.4. This non-monotonic behavior is of course related to the mixing properties, which are different depending on the flow structure.

PLIF measurements allow to visualize the motion and the time-evolution of a fluorescent tracer, within and across the vortices. From these results, the mixing properties were quantified using a mixing index (intensity of segregation), noted *I*, over the different directions and between adjacent vortices. We have considered three adjacent vortices A, B and C, as depicted in Fig. 11. A stands for the vortex in which the dye is injected, B for the outflow-adjacent vortex to A, and C is the inflow-adjacent vortex to A. Detailed investigation of the mixing properties and technical issues are given in Nemri et al. (2014).

In order to study the effect of the wave state on intra and intervortex mixing, various wave states were considered at Reynolds $Re = 1082$. These particular flow regimes were achieved using the various acceleration protocols described in Section 3.1. The results are plotted in terms of the intensity of segregation, *I*,

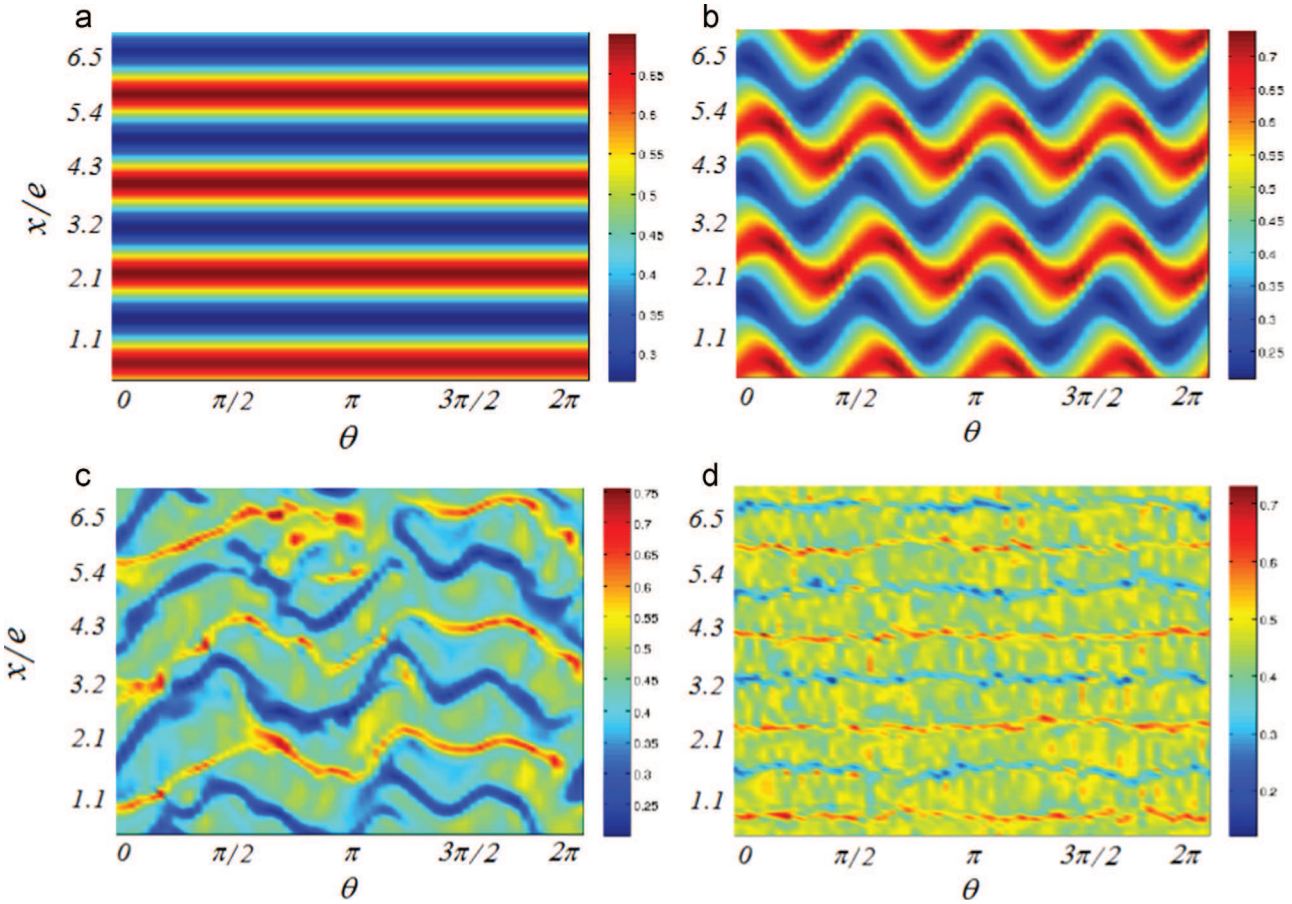

Fig. 7. DNS visualization of the flow regimes achieved in the small-gap column ($\eta = 0.85$) – Isocontours of the axial velocity in the middle of the gap $r = (1+\eta)/2$. (a) $Re = 140$ (TVF). (b) $Re = 200$ (WVF). (c) $Re = 800$ (MWVF). (d) $Re = 3500$ (TTVF).

either between adjacent vortices or within a given vortex, for three different wave states.

I_v quantifies the intervortex exchange between adjacent vortices A and B and is defined by $I_v = \frac{\sigma_c^2}{\sigma_0^2}$, with σ_c the standard deviation of tracer concentration and σ_0 the maximum mean concentration

$$\begin{cases} \sigma_c^2 = \dfrac{1}{N-1}\sum (C_A - \overline{C})^2 \\ \sigma_0^2 = \overline{C}(1-\overline{C}) \\ \overline{C} = \dfrac{\sum C}{N} \end{cases} \tag{7}$$

C_A is the average concentration over the spatial region occupied by vortex A (it has been scaled by C_0 the concentration of injected tracer) and $\overline{C}$ is the average normalized concentration over the two adjacent vortices ($C = (C_A + C_B)/2$), formed over N time frames.

I_{rz} and I_θ quantify the intravortex mixing respectively in the meridional plane (by considering the average concentration over one period) and in the azimuthal direction (by considering the average concentration over the $r-z$ plane).

As illustrated by Figs. 11 and 12, I_v, I_{rz} and I_θ approach zero when the perfectly mixed state is reached.

The plots in Fig. 11 show that intervortex mixing is significantly influenced by the wave state (values of λ_x and m). We can also

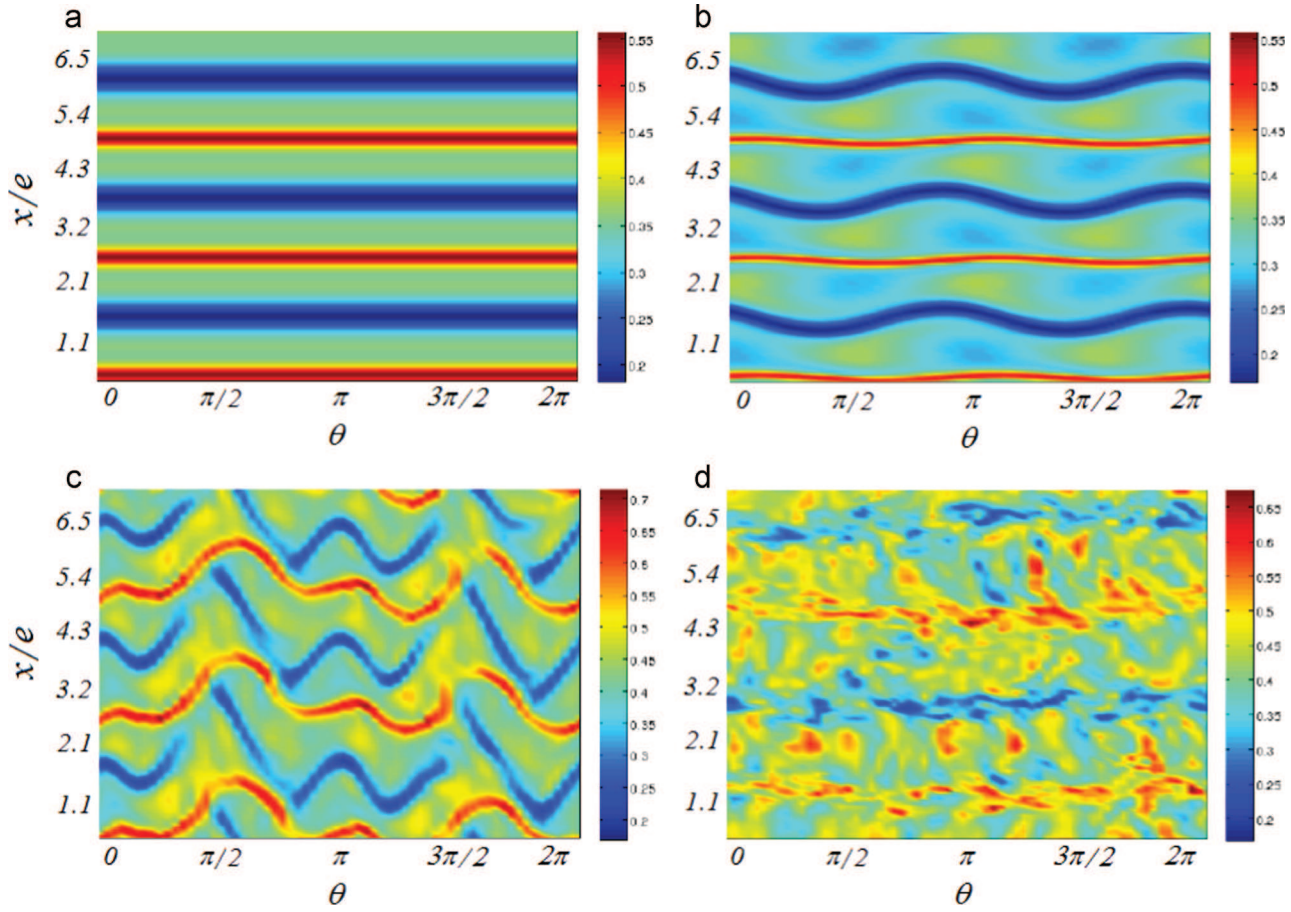

Fig. 8. DNS visualization of the flow regimes achieved in the large-gap column ($\eta = 0.687$) – Isocontours of the axial velocity in the middle of the gap $r = (1+\eta)/2$. (a) Re = 318 (TVF). (b) Re = 953 (WVF). (c) Re = 1980 (MWVF). (d) Re = 4000 (TTVF).

Table 3
Flow transitions.

Geometry	Transition to TVF	Existence of WVF
$\eta = 0.85$	$Re_c = 125$	$165 < Re < 680$
$\eta = 0.687$	$Re_c = 79$	$387 < Re < 1793$

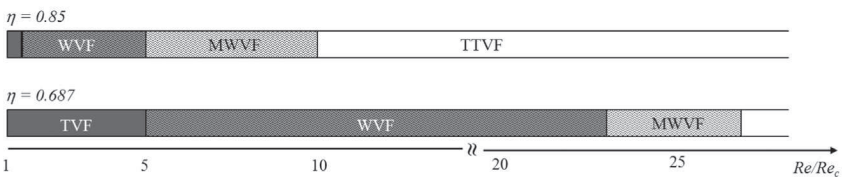

Fig. 9. Observed flow map from TVF to turbulence and range of existence of the wavy regimes (WVF: dark wavy pattern and MWVF light wavy pattern).

notice that the mixing time-scale decreases with the axial wavelength. For instance, for $\lambda_x = 2.35e$, the time-scale for perfect mixing over the outflow boundaries is estimated to be twice larger than for the case $\lambda_x = 2.4e$ and three times larger than for $\lambda_x = 2.47e$. Indeed, longer axial wavelength leads to greater distance traveled by the passive tracer in each vortex.

Similarly, we observed that in the inflow zone, the mass transport is enhanced for flows where the amplitude of the traveling wave is large. When the outflow boundaries are modulated by the wavy perturbation ($\lambda_x = 2.47e$ with $m=3$), the rate of mass transfer increases dramatically compared to cases of weakly rippling outflow zones ($\lambda_x = 2.35e$ and $\lambda_x = 2.4e$ where $m=1$ at the outflow boundary). Moreover, in the case $\lambda_x = 2.47e$, the wave number is $m=3$ in both the inflow and outflow boundaries, thus resulting in an enhanced exchange between neighboring vortices and consequently an enhanced axial dispersion.

On the other hand, however, the results did not reveal obvious influence of the multiplicity of wave states on intravortex mixing (Fig. 12). The degree of intravortex mixing increases with *Re*, over the range we have studied, regardless of the wave state. Actually, intravortex mixing is mainly controlled by the velocity field and its gradients which increase the vortex capability to stretch and transport the dye. This could explain why for higher Reynolds the wave state effect appears negligible. This observation is in agreement with the study of Ohmura et al. (1997), who showed a weak influence of the wave-state on intravortex mixing.

In summary, PLIF results highlight the relation between the mixing properties and the flow wave-state. Intervortex mixing is indeed significantly influenced by the wave-state, and particularly by the axial wavelength λ_x and the wave amplitude. This behavior explains the scattering observed at the macroscopic level in terms of dispersion coefficient D_x.

4.5. DNS investigation of mixing mechanisms

In this section, we investigate more systematically mixing by tracking computationally fluid particles trajectories. The evolution of the flow field and the particles trajectories are simultaneously integrated forward in time. This approach was used by many authors, e.g. Rudman (1998), King et al. (2001) while Akonur and Lueptow (2002) have used measured velocity fields (by PIV) as the carrying Eulerian flow to calculate particle trajectories.

After the flow transient toward the desired wave-state (see Section 3.2), a large amount of particles (about 1000 to 10,000) are injected at a specified axial position. Calculations were carried out for two different Reynolds numbers associated to TVF and WVF regimes. For each *Re*, particles were injected at three different locations: the vortex center, the inflow zone and the outflow zone, respectively.

The streaklines of the particles in TVF regime ($Re=318$) are shown in Fig. 13. Most of the particles that were initially seeded at the vortex center are observed to remain trapped into the vortices core, and their trajectories exhibit a spiral structure. Hence, particles near the vortex cores, where the velocity and its gradients are weak, continue to move in the azimuthal direction, though they are still trapped in the same vortex. This confirms that mixing in TVF is weak in agreement with PLIF measurements.

Intervortex transport toward adjacent vortices is basically initiated by molecular diffusion across cell boundaries. However, snapshots of particle paths exhibit that particles initially located between adjacent vortices (inflow and outflow zones) have different trajectories and have more chance to be transported from one vortex to the neighboring one. Though, intervortex mixing remains weak.

In WVF regime, as mentioned previously, the appearance of the traveling wave breaks the boundaries between vortices. The flow becomes more chaotic which greatly increases its capacity to advect, stretch and diffuse the passive tracer, in agreement with the experimental observations (PLIF and RTD). The same observation can be made from our DNS. Particle streaklines presented in Figs. 14 and 15 show that the transport of particles tracer between vortices becomes more effective.

As in TVF, the initial distribution of particles influences significantly the particles trajectories in WVF regime. Particles seeded at the vortex boundaries are more likely to be transported along the axial direction through vortices. This was also observed in our mixing measurements in terms of intervortex mixing. Intervortex mixing across inflow boundaries was more efficient than through outflow boundaries due to the velocity field characteristics in these two zones (see Section 4.2 and details in Akonur and

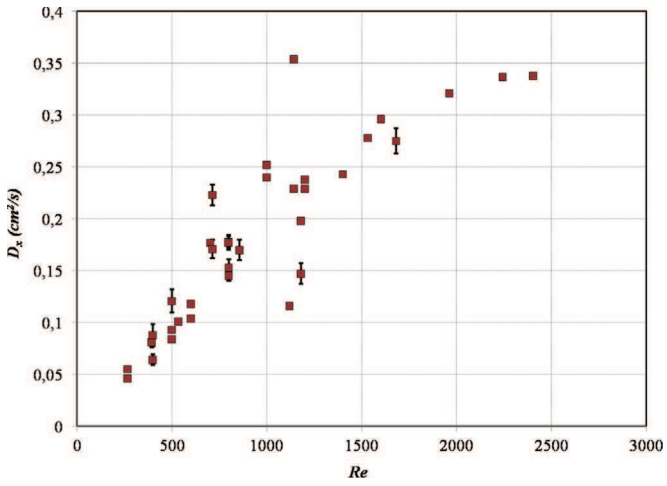

Fig. 10. Dispersion coefficient D_x as a function of *Re* ($\eta = 0.85$).

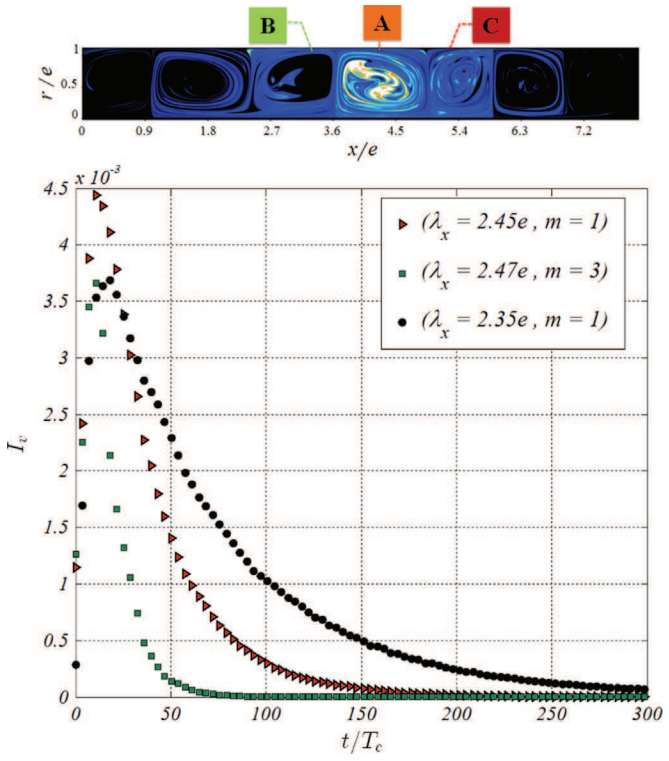

Fig. 11. Intervortex mixing between vortex A and B (outflow zone), influence of the wave state ($Re=1082$) – $T_c = 0.9$ s is the rotation period of the inner cylinder.

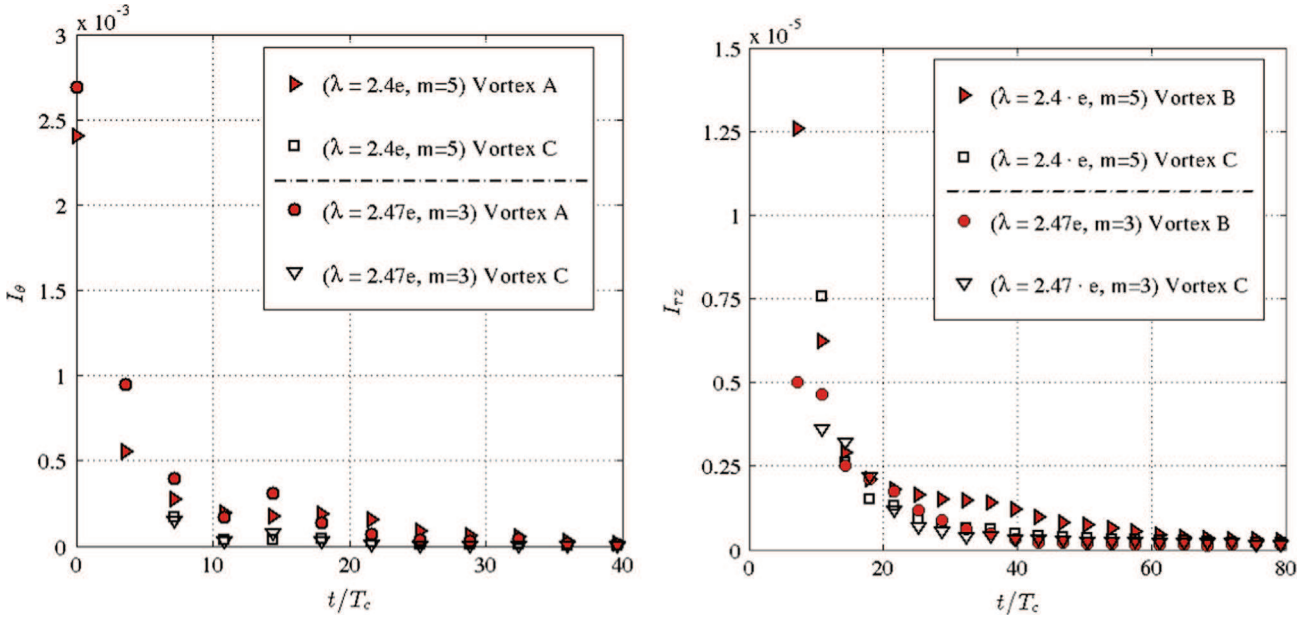

Fig. 12. Wave state effect on Intravortex mixing in the azimuthal direction (left) and in the meridional plane (right) at $Re=1082$.

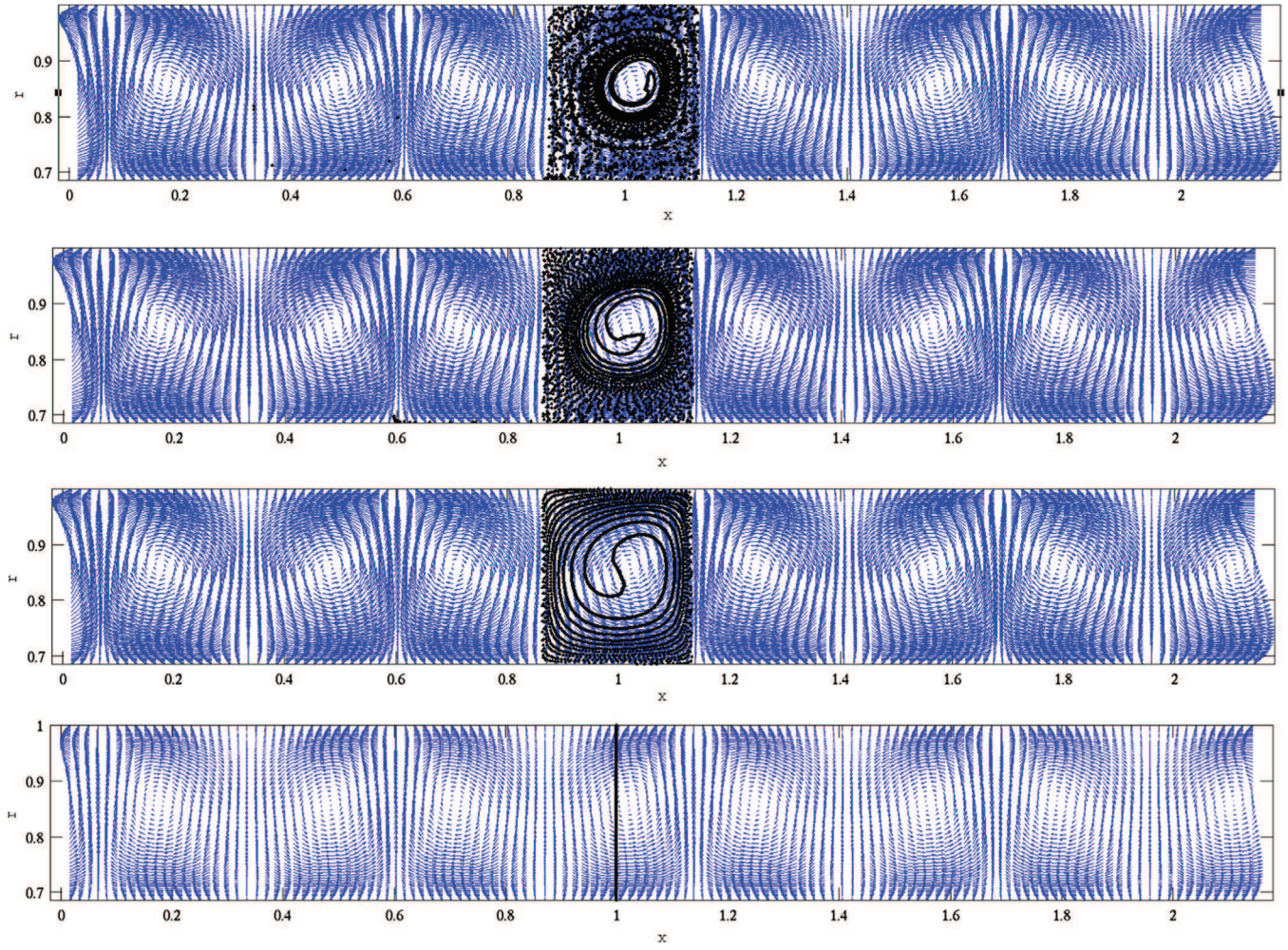

Fig. 13. Deformation of a line of 5000 particles initially seeded across the vortex center as a function of time ($Re=318$). From left to right: $t=0$, $t=2T_c$, $t=4T_c$, $t=8T_c$ while $T_c=3$ s corresponds to the rotation period. (2D view, x and y axis are in dimensionless units that respectively correspond to e and 4λ.)

Lueptow, 2002). This enhancement of the mass-transport process between vortices results in an increase of the axial dispersion coefficient. These observations are in agreement with previous analysis from Desmet et al. (1996a) and Desmet et al. (1996b).

4.6. The effect of the wave-state on axial dispersion

Based on the study of the mixing mechanisms, we intend to use the results at the local scale to explain the scattering observed in

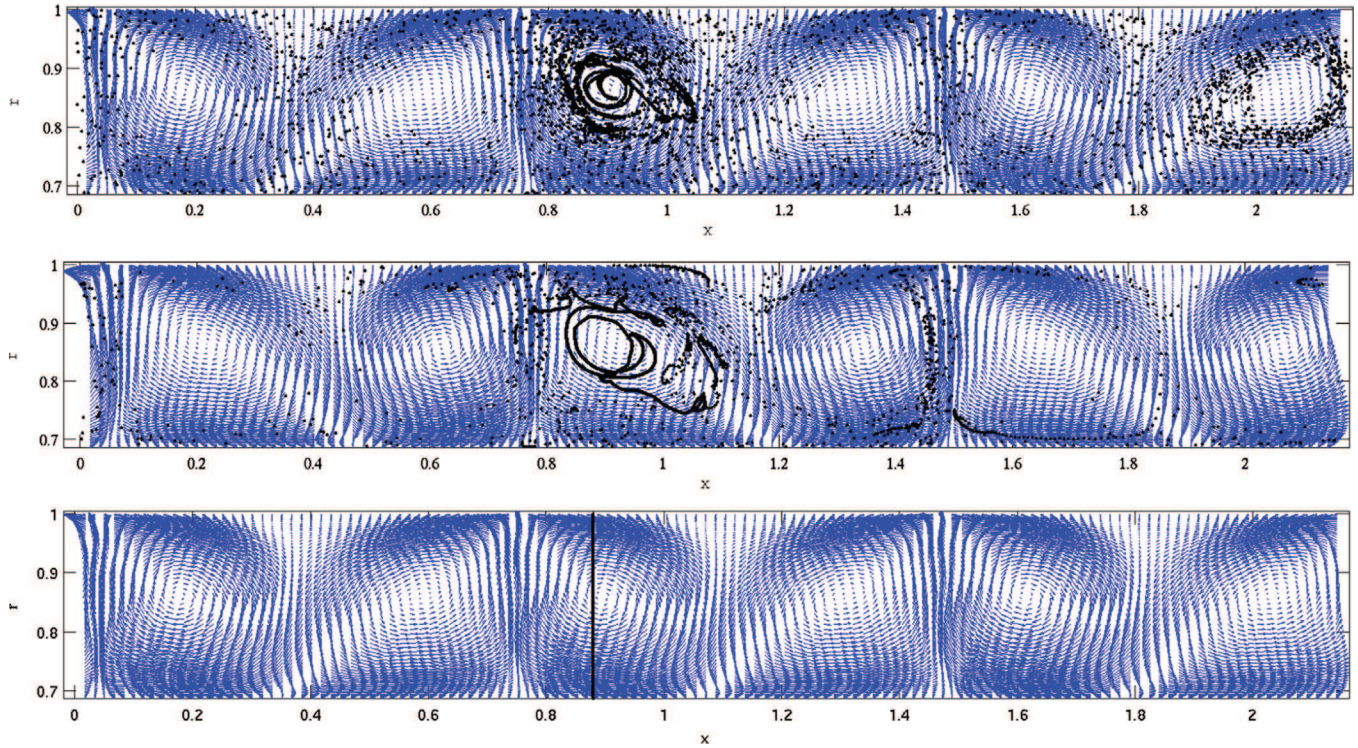

Fig. 14. Deformation of a line of 5000 particles initially seeded across the vortex center as a function of time (Re=1192). From left to right: t=0, $t=2T_c$, $t=8T_c$ while T_c=0.8 s corresponds to the rotation period. (2D view, x and y axis are in dimensionless units that respectively correspond to e and 4λ.)

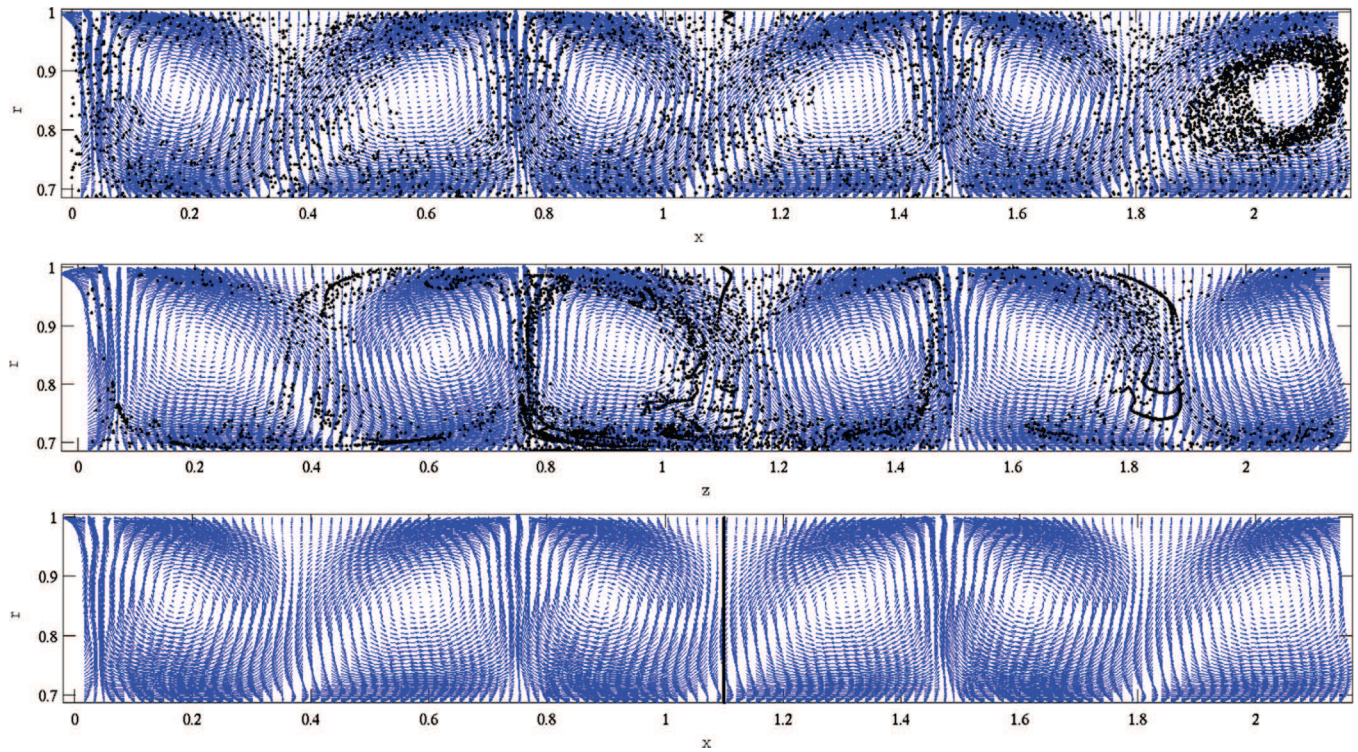

Fig. 15. Deformation of a line of 5000 particles initially seeded at the inflow zone between two adjacent vortices as a function of time (Re=1192). From left to right: t=0, $t=2T_c$, $t=8T_c$ while T_c=0.8 s corresponds to the rotation period. (2D view, x and y axis are in dimensionless units that respectively correspond to e and 4λ.)

the measured dispersion coefficients at the macroscopic scale. Additional RTD measurements were performed. Specific start-up protocols were used in order to control the achieved wave-state and guarantee the reproducibility of the measurements. The results are illustrated in Fig. 16, which exhibits an excellent agreement with the observations at local scale (PLIF and DNS). The transition to WVF regime significantly enhances axial dispersion and scattering of D_x.

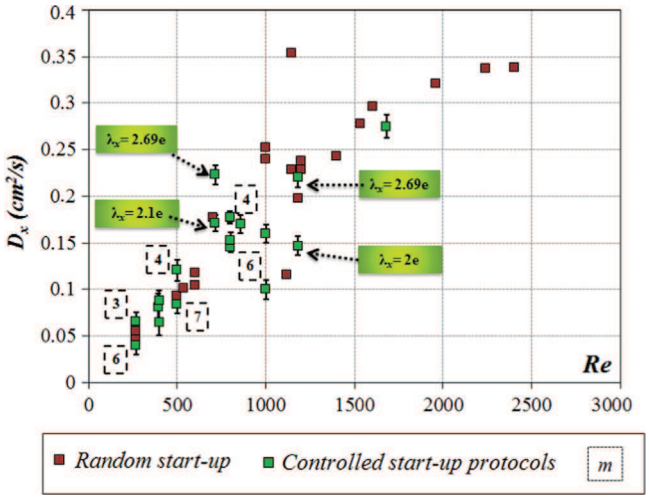

Fig. 16. Dispersion coefficient D_x as a function of Re ($\eta = 0.85$) – Influence of the flow state.

Furthermore, the same tendency is observed regarding the influence of the wave state (Fig. 17): the axial dispersion coefficient is clearly an increasing function of the axial wavelength λ_x, which is in agreement with the observed increase of intervortex mixing. This trend was also observed by Rudman (1998) and Rudman et al. (2008) for wavy regimes. At last, experimental (RTD) and numerical D_x results are compared quantitatively in Fig. 17. The agreement is good, which confirms the strong correlation between the wave state, mixing efficiency and passive tracer dispersion.

In order to explore this point in details, additionnal DNS simulations were carried out and different wave states, which were not achieved in our experiments, were examined for several Reynolds numbers. Actually, DNS provides easily access to various wave states as explained in Section 3.2. Two categories of simulations were carried out:

- In Fig. 18, the azimuthal wave number m was fixed and the axial wavelength λ_x was varied. The effect of the wavelength is monotonous as longer vortices enhance axial dispersion for a giver Reynolds number.

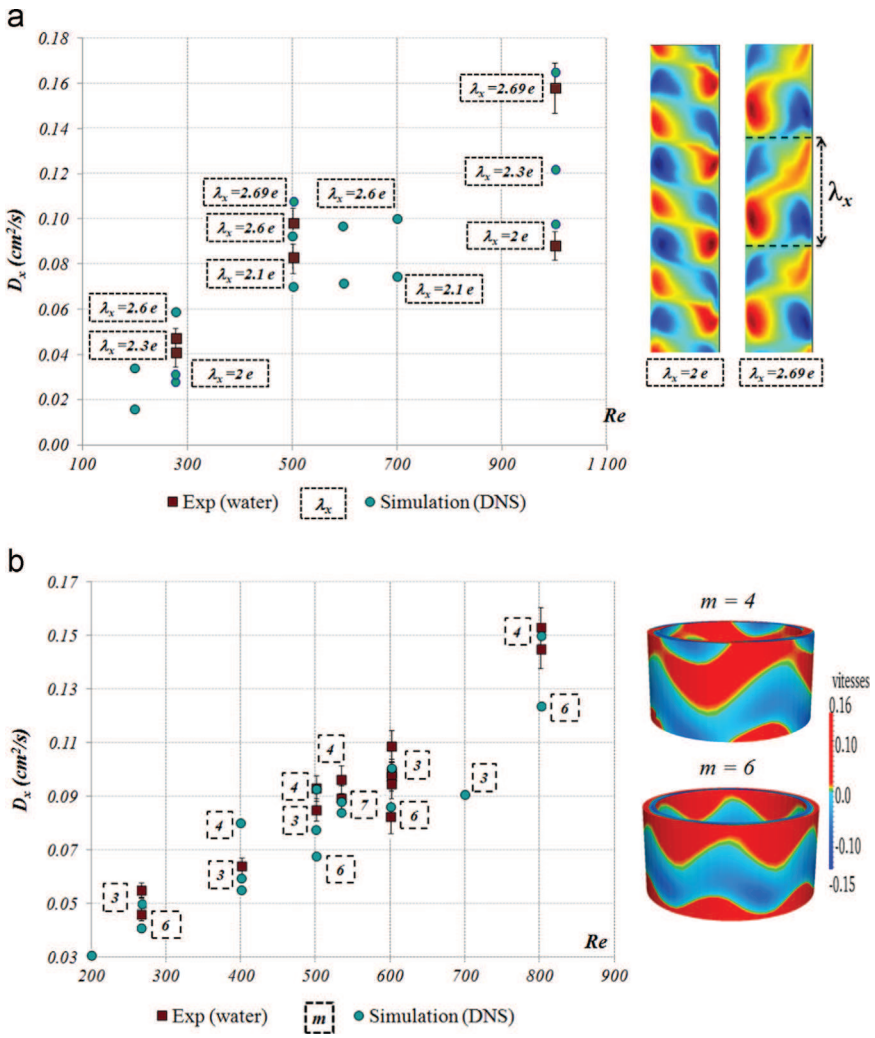

Fig. 17. Evolution of the axial dispersion coefficient: comparison of experimental and numerical values for $\eta = 0.85$. Top: influence of the axial wavelength λ_x (m=4 in each case) – Bottom: influence of the azimuthal wave number m (axial wavelength in the range $2.6e \leq \lambda_x \leq 2.69e$).

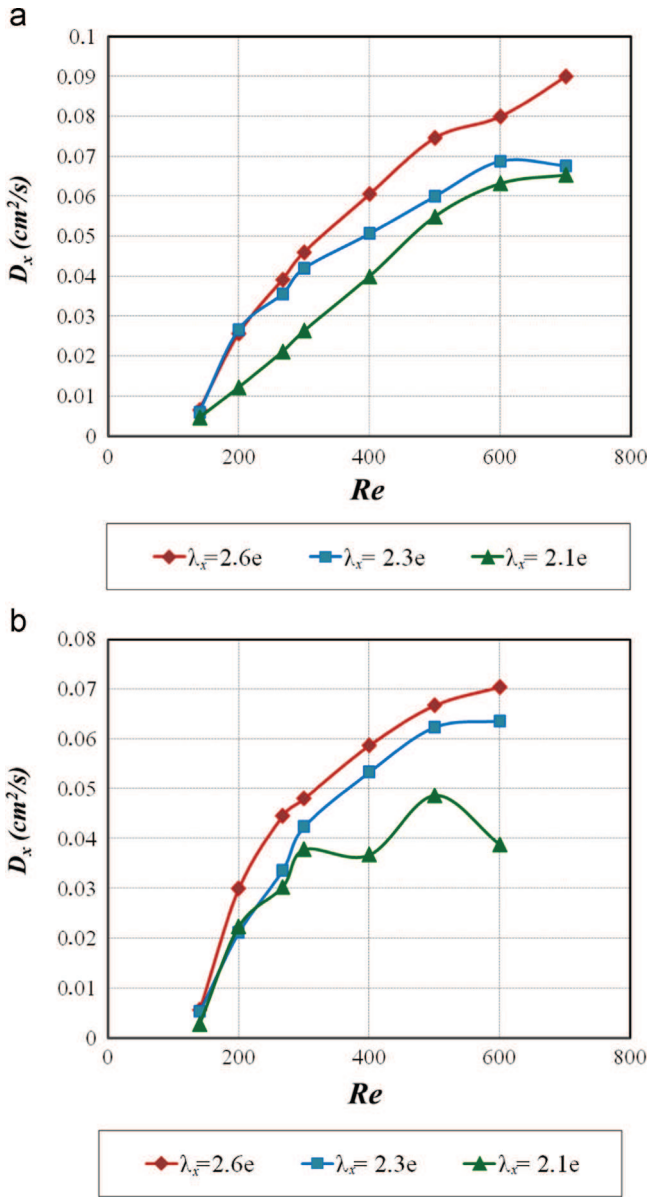

Fig. 18. Dispersion coefficient D_x as a function of Re and axial wavelength λ_x for a fixed azimuthal wavenumber m ($\eta = 0.85$) – (a) $m=3$, (b) $m=6$.

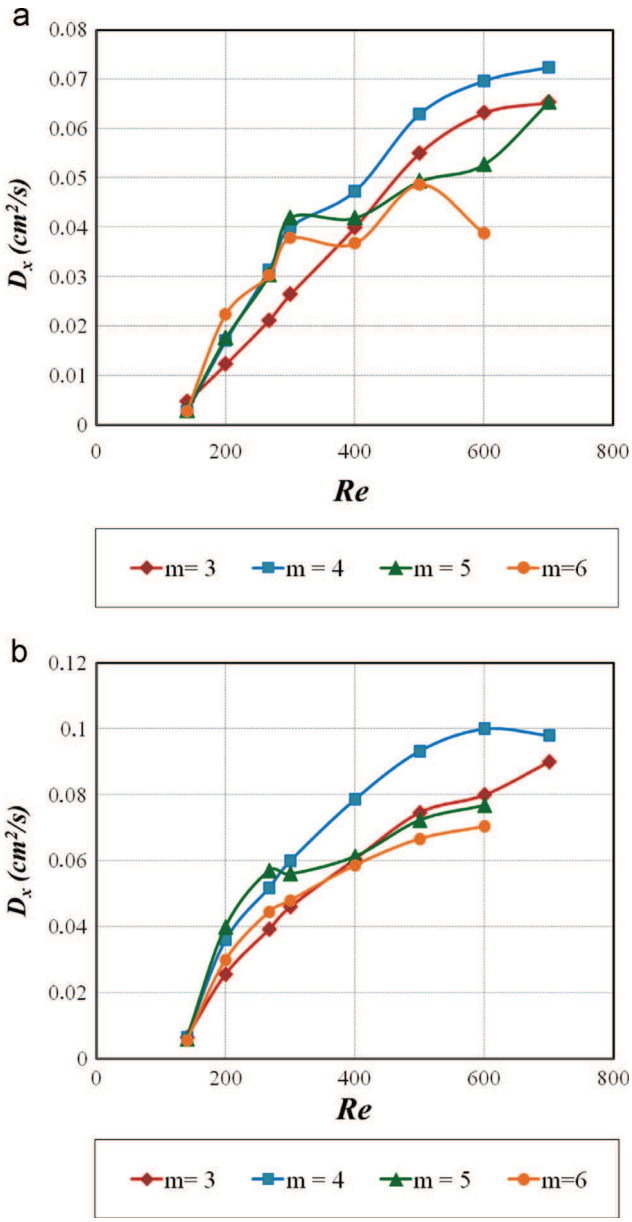

Fig. 19. Dispersion coefficient D_x as a function of Re and azimuthal wavenumber m for a fixed axial wavelength λ_x ($\eta = 0.85$) – (a) $\lambda_x = 2.1e$, (b) $\lambda_x = 2.6e$.

- Then, λ_x was fixed and m was varied (Fig. 19). The results show that no obvious correlation can be made from the wave state and the mixing efficiency.

These additional numerical results confirm experimental evidences, especially regarding the effect of λ_x. For the same Reynolds number, increasing λ_x results in an increased D_x.

5. Conclusion

We mainly focused on the dynamics of Wavy Vortex Flow in Taylor–Couette geometry and its relation with the axial dispersion of a passive tracer. Thanks to simultaneous PIV–PLIF visualizations and RTD measurements complemented with DNS simulations, the influence of the successive flow bifurcations and wave states on axial dispersion was investigated. The numerical results confirm that, in the range of regimes we considered, the scattering of dispersion coefficient (typically a factor two) is indeed the consequence of the occurrence of various wave-states for the same Reynolds number. Numerical and experimental results are in agreement and show that longer axial wavelengths and lower azimuthal wavenumbers result in larger axial dispersion. Indeed, as evidenced by the PLIF measurements, a longer axial wavelength means a greater distance traveled by the fluid tracer in each vortex hence, as intervortex mixing is dominant, fluid elements are expected to be transported more efficiently resulting in an enhanced axial dispersion. On the other hand, the effect of various wavenumbers does not follow an obvious trend which can explain why obtaining universal correlations may fail.

In terms of macroscopic analysis, different flow states have been investigated systematically by DNS and quantitatively compared to experiment RTD measurements. Our study confirms that commonly used chemical engineering models (a non exhaustive list is given in Table 1) are very limited to characterize axial dispersion in Taylor–Couette flows beyond the wavy regime. Indeed, the flow structure is non-unique for this range of Reynolds number while many azimuthal wavenumbers and axial wavelengths

may occur yielding non-monotonous evolution of the mixing efficiency.

PLIF visualizations showed clear evidences of different transport mechanisms including "intra-vortex mixing" and "inter-vortex mixing". Under wavy flow regimes, intra-vortex mixing is controlled by chaotic advection, due to the 3D nature of the flow, while inter-vortex transport occurs due to the presence of waves between neighboring vortices as observed by Akonur and Lueptow (2002). The combination of these two mechanisms results in enhanced axial dispersion. The evolution of axial dispersion coefficient D_x along the successive flow states was investigated thanks to dye Residence Time Distribution measurements (RTD) and particle tracking in numerical flow simulations. We showed that hysteresis may occur between consecutive regimes depending on flow history and this has a significant effect on mixing efficiency for a given Reynolds number.

Our study provides new information on the interplay between local flow properties, tracer transport and a macroscopic measure of mixing such as axial dispersion. Although the major role of the axial wavelength was confirmed, it is still unclear which theoretical modeling is appropriate to obtain reliable prediction of dispersion for specific geometric configurations and operating conditions.

Nomenclature

Variables

C	dimensionless concentration (–)
$\overline{C}$	mean concentration (–)
C_0	injection concentration ($g\,L^{-1}$)
D_x	axial dispersion coefficient ($m^2\,s^{-1}$)
e	annular gap width (m)
I	intensity of segregation (–)
I_{rz}	intensity of segregation in the meridional plane (r–z) (–)
I_θ	intensity of segregation in the azimuthal direction (θ) (–)
I_v	intensity of segregation between adjacent vortices (–)
L	column height (m)
m	Azimuthal wave number (–)
P	pressure (Pa)
R	radius (m)
Re, Re_{ax}	tangential Reynolds number, axial Reynolds number (–)
T_c	inner cylinder rotational period (s)
u, U	velocity ($m\,s^{-1}$)
λ_x	axial wavelength (m)
η	radius ratio (–)
μ	dynamic viscosity (Pa s)
ν	kinematic viscosity ($m^2\,s^{-1}$)
ρ	density ($kg\,m^{-3}$)
Γ	column aspect ratio (–)
Ω	inner cylinder rotational speed (s^{-1})

Abbreviations

CSTR	Continuously Stirred Tank Reactors in series
CFL	Courant number (Courant–Friedrichs–Lewy)
DNS	Direct Numerical Simulation
PFD	Plug Flow with axial Dispersion
PIV	Particle Image Velocimetry
PLIF	Planar Laser Induced Fluorescence
RTD	Residence Time Distribution
TVF	Taylor Vortex Flow
WVF	Wavy Vortex Flow
MWVF	Modulated Wavy Vortex Flow
TTVF	Turbulent Taylor Vortex Flow

Subscripts

c	Critical
i	Inner cylinder
e	Outer cylinder
r	Radial direction
θ	Azimuthal direction
x	Axial direction
r–x	Meridional plane
0	Initial condition

Acknowledgments

The authors would like to thank S. Cazin and M. Marchal, from IMFT, and F. Lamadie, from CEA Marcoule, for technical support during experiments and fruitful discussions.

References

Akonur, A., Lueptow, R., 2002. Chaotic mixing and transport in wavy Taylor–Couette flow. Physica D 167, 183–196.

Andereck, D., Liu, S., Swinney, H., 1985. Flow regimes in a circular Couette system with independently rotating cylinders. J. Fluid Mech. 164, 155–183.

Bilson, M., Bremhorst, K., 2007. Chaotic mixing and transport in wavy Taylor–Couette flow. J. Fluid Mech. 579, 227–270.

Calmet, I., Magnaudet, J., 1997. Large-eddy simulation of high-Schmidt number mass transfer in a turbulent channel flow. Phys. Fluids 9, 438–455.

Campero, R., Vigil, R., 1997. Axial dispersion during low Reynolds number Taylor–Couette flow: intra vortex mixing effect. Chem. Eng. J. 52, 3305–3310.

Chouippe, A., Climent, E., Legendre, D., Gabillet, C., 2014. Numerical simulation of bubble dispersion in turbulent Taylor–Couette. Phys. Fluids 26, 043304.

Climent, E., Magnaudet, J., 1999. Large-scale simulations of bubble-induced convection in a liquid layer. Phys. Rev. Lett. 82, 4827.

Coles, D., 1965. Transitions in circular Couette flow. J. Fluid Mech. 21, 385–425.

Davis, M., Weber, E., 1960. Liquid–liquid extraction between rotating concentric cylinders. Ind. Eng. Chem. 52, 929–934.

Desmet, G., Verelst, H., Baron, G., 1996a. Local and global dispersion effect in Couette–Taylor flow - I. Description and modeling of the dispersion effects. Chem. Eng. J. 51, 1287–1298.

Desmet, G., Verelst, H., Baron, G., 1996b. Local and global dispersion effect in Couette–Taylor flow - II: quantative measurements and discussion of the reactor performance. Chem. Eng. J. 51, 1299–1309.

DiPrima, R., Eagles, P., Ng, B., 1984. The effect of radius ratio on the stability of Couette flow and Taylor vortex flow. Phys. Fluids 27 (10), 2403–2411.

Dusting, J., Balabani, S., 2009. Mixing in Taylor–Couette reactor in the non wavy flow regime. Chem. Eng. Sci. 64, 3103–3111.

Dutcher, C., Muller, S.J., 2009. Spatio-temporel mode dynamics and higher order transitions in high aspect ratio Newtonian Taylor–Couette flow. J. Fluid Mech. 641, 85–113.

Enkoida, Y., Nakata, K., Suzuki, A., 1989. Axial turbulent diffusion in fluid between rotating coaxial cylinders. AIChE J. 35 (7), 1211–1214.

Fenstermacher, P., Swinney, H., Gollub, J., 1979. Dynamical instabilities and the transition to chaotic Taylor vortex flow. J. Fluid Mech. 94, 103–127.

Guihard, I., Coeuret, F., Legrand, L., Fahidy, T., Gu, Z., 1989. Circumferential mixing in the Taylor–Couette reactor. Chem. Eng. Symp. Ser. 112, 105–117.

Haut, B., Amor, H., Coulon, L., Jacquet, A., Halloin, V., 2003. Hydrodynamics and mass transfer in a Couette–Taylor bioreactor for the culture of animal cells. Chem. Eng. J. 58, 777–784.

Hill, E., Krebs, B., Goodall, D., Howlett, G., Dunstan, D., 2006. Shear flow induces amyloid fibril formation. Biomacromolecules 7, 10–13.

Kataoka, K., Doi, H., Komai, T., 1977. Heat and mass transfer in Taylor-vortex flow with constant axial flow rate. Int. J. Heat Mass Transf. 57, 472–476.

Kataoka, K., Hongo, T., Fugatawa, M., 1975. Ideal plug-flow properties of Taylor-vortex flow. J. Chem. Eng. Jpn. 8, 472–476.

Kataoka, K., Ohmura, N., Kouzu, M., Simamura, Y., Okubu, M., 1995. Emulsion polymerization of styrene in a continuous Taylor vortex flow reactor. Chem. Eng. Sci. 50, 1409–1416.

Kataoka, K., Takigawa, T., 1981. Intermixing over cell boundary between Taylor vortices. AIChE J. 27, 504–508.

King, G., Rowlands, G., Rudman, M., Yannacopoulos, A., 2001. Predicting chaotic dispersion with Eulerian measures: wavy Taylor vortex flow. Phys. Fluids 13, 2522.
Lanoë, J.Y., 2002. Performances d'une colonne d'extraction liquide-liquide miniature basée sur un écoulement de Taylor–Couette, in: ATALANTE Conference.
Legrand, J., Coeuret, F., Billon, M., 1983. Structure dynamique et transfert de matière liquide-paroi dans le cas de l'écoulement laminaire tourbillonnaire de Couette–Poiseuille. Int. J. Heat Mass Transfer 48, 1075–1085.
Legrand, J., Coeuret, F., 1986. Circumferentional mixing in one phase and two-phase Taylor vortex flow. Chem. Eng. J. 41, 47–53.
Moore, C., Cooney, C., 1995. Axial dispersion in Taylor–Couette flow. AIChE J. 41, 723–727.
Nemri, M., Cazin, S., Charton, S., Climent, E., 2014. Experimental investigation of mixing and axial dispersion in Taylor–Couette flow patterns. Exp. Fluids 55 (7), 1769.
Nemri, M., Charton, S., Climent, E., Lanoë, J., 2013. Experimental and numerical investigation on mixing and axial dispersion in Taylor–Couette flow patterns. Chem. Eng. Res. Des. 91 (12), 2346–2354.
Ohmura, N., Kataoka, K., Shibata, Y., Makino, T., 1997. Effective mass diffusion over cell boundaries in Taylor–Couette flow system. Chem. Eng. J. 52 (11), 1757–1765.
Pudijioni, P., Tavare, N., Garside, J., Nigam, K., 1992. Residence time distribution from a continuous Couette flow device. Chem. Eng. J. 48, 101–110.
Racina, A., Liu, Z., Kind, M., 2010. Mixing in Taylor–Couette Flow. Springer, Berlin, pp. 125–139.
Raguin, L., Shannon, M., Georgiadis, J., 2001. Dispersion radiale et axiale dans les écoulements tourbillonnaires de type Taylor–Couette. Int. J. Heat Mass Transf. 44 (17), 3295–3306.
Rudman, M., 1998. Mixing and particle dispersion in the wavy vortex regime of Taylor–Couette flow. AIChE J. 44, 1015–1026.
Rudman, M., Metcalfe, G., Lachlan, J., Graham, W., 2008. Nonmixing vortex cores in wavy Taylor vortex flow. Phys. Fluids 20, 063602.
Tam, W., Swinney, H., 1987. Mass transport in turbulent Taylor–Couette flow. Phys. Rev. A 36, 1374–1381.
Villermaux, J., Genie de la reaction chimique, 2nd ed., Tec ed Doc Lavoisier, 1993.
Wereley, S., Lueptow, R. Velocity field for Taylor–Couette flow with an axial flow, Phys. Fluids 11, 1999.
Zhu, X., Campero, R., Vigil, D., 2000. Axial mass transport in liquid–liquid Taylor–Couette–Poiseuille flow. Chem. Eng. Sci. 55, 5079–5087.